


PAPER • OPEN ACCESS

Rapid subsurface damage detection of SiC using inductivity coupled plasma

To cite this article: Yi Zhang *et al* 2021 *Int. J. Extrem. Manuf.* **3** 035202

View the [article online](#) for updates and enhancements.

Rapid subsurface damage detection of SiC using inductivity coupled plasma

Yi Zhang^{1,2}, Linfeng Zhang¹, Keyu Chen¹, Dianzi Liu², Dong Lu¹ and Hui Deng^{1,*} 

¹ Department of Mechanical and Energy Engineering, Southern University of Science and Technology, No. 1088, Xueyuan Road, Shenzhen, Guangdong 518055, People's Republic of China

² School of Engineering, Faculty of Science, University of East Anglia, Norwich Research Park, Norwich NR4 7TJ, United Kingdom

E-mail: dengh@sustech.edu.cn

Received 2 January 2021, revised 7 February 2021

Accepted for publication 8 May 2021

Published 24 May 2021



CrossMark

Abstract

This paper proposes a method for the rapid detection of subsurface damage (SSD) of SiC using atmospheric inductivity coupled plasma. As a plasma etching method operated at ambient pressure with no bias voltage, this method does not introduce any new SSD to the substrate. Plasma diagnosis and simulation are used to optimize the detection operation. Assisted by an SiC cover, a taper can be etched on the substrate with a high material removal rate. Confocal laser scanning microscopy and scanning electron microscope are used to analyze the etching results, and scanning transmission electron microscope (STEM) is adopted to confirm the accuracy of this method. The STEM result also indicates that etching does not introduce any SSD, and the thoroughly etched surface is a perfectly single crystal. A rapid SSD screening ability is also demonstrated, showing that this method is a promising approach for the rapid detection of SSD.

Keywords: silicon carbide, subsurface damage, SSD detection, ICP etching

1. Introduction

Single crystal silicon carbide (4H-SiC) is considered one of the most promising third-generation semiconductor materials with applications in many cutting-edge fields, including electronics, optics, and graphene growth [1]. 4H-SiC has many excellent properties, such as a wide bandgap, low thermal expansion coefficient, high specific stiffness, good size stability, and high radiation resistance [2, 3]. Despite these advantages, 4H-SiC is a typical difficult-to-machine material because of its high hardness and strong chemical inertness [4, 5]. Furthermore, subsurface damage (SSD) is more easily introduced into this type of hard and brittle material during the machining process. SSD impairs the mechanical, electronic, and optical

properties of materials [6–8]. Thus, it is necessary to remove all SSD for advanced applications.

As a typical difficult-to-machine material, the processing of SiC wafers usually takes hours, especially the last polishing step, which removes all SSD introduced by previous slicing, grinding, and lapping steps [9]. The typical material removal rate (MRR) of SiC via the chemical mechanical polishing (CMP) method is $\sim 100 \text{ nm h}^{-1}$ [10]. Moreover, this process consumes a large amount of slurry, which can be toxic, contaminative, and expensive [11, 12]. To minimize the duration of CMP, a precision measurement method of the SSD layer thickness is indispensable.

SSD can be detected using destructive and nondestructive methods. Destructive methods include taper polishing, cross-sectional microscopy, and etching, while nondestructive methods include x-ray scanning, laser scattering, and ultrasonic probing [13]. A nondestructive method can achieve in-process detection and will not destroy the sample. However, the detection accuracy and efficiency are relatively low. Destructive methods, in contrast, are more mature and have better reliability and accuracy. Thus, this type of method is widely

* Author to whom any correspondence should be addressed.



Original content from this work may be used under the terms of the [Creative Commons Attribution 3.0 licence](https://creativecommons.org/licenses/by/3.0/). Any further distribution of this work must maintain attribution to the author(s) and the title of the work, journal citation and DOI.

used in industry and academia at present [13]. The most widely used destructive method is taper polishing, which is based on removing the material to form a taper or dimple that crosses the SSD layer to the damage-free matrix and observing the revealed surface to measure the SSD thickness [14]. To operate destructive SSD detection methods, a material removal method that does not introduce new SSD is indispensable. Conventional methods that meet this demand have been applied in SSD detection including CMP, chemical etching, and magnetorheological finishing (MRF) [15–17]. For CMP, the main drawback is the low MRR for SiC and the massive consumption of slurry, which is expensive and toxic [10–12]. Chemical etching uses hydrofluoric acid (HF) solution, which is hypertoxic. In addition, SiC does not react with HF at room temperature because of its excellent chemical inertness [18]. Among the destructive methods, MRF is most widely used. However, MRF often introduces Fe contamination into the sample [19]. Moreover, the MRR is not very high for SiC, and the general MRR is below $0.2 \mu\text{m min}^{-1}$ [20]. To increase the MRR of MRF, diamond abrasives are often used, which might introduce new damage [21]. Furthermore, MRF needs to collocate with a subsequent etching step to open cracks [13]. This etching step will be difficult for SiC because it is inert in all known aqueous etching solutions at room temperature [18]. To further develop the SSD detection technique, a novel SSD-free material removal method is needed.

Plasma etching is generally considered an ‘ion-assisted gas-surface chemistry mechanism’ process, and ion bombardment is the main cause of plasma-induced damage. However, damage induced by atmospheric pressure inductively coupled plasma etching (ICPE) can be very low. ICP can achieve a higher etching rate under no substrate bias because of the much higher ion-to-neutral flux ratio and a much larger active species production rate compared to capacitively coupled plasma [22]. Furthermore, the incident energy for atmospheric ICP can be even lower because of the short mean free path; thus, the etching process is free of structural damage [23]. Recently, the application of atmospheric ICP as a potentially efficient machining method has been studied by many researchers. For instance, reactive atom plasma technology by Fanara *et al*, atmospheric pressure plasma polishing by Jin *et al*, and ICPE by Dai *et al* have achieved SSD-free processing of fused silica based on ICPE [24–26]. Furthermore, Dai *et al* discussed the surface damage evolution of fused silica under ICPE and compared it with that of the MRF method, implying that ICP could be a promising method for SSD detection [26].

Precision detection of SSD using ICPE is difficult because the etching spot is relatively large, in the range of centimeters. The spread radicals reach an even larger area, resulting in whole surface etching. Meanwhile, the deposition of fluorocarbon particles covers the original surface. It is imprecise to measure the SSD thickness by comparing the last trace of the SSD layer and the remainder of the surface. Meanwhile, confocal microscopy for large areas loses accuracy because of pixel-limited resolution [27]. In this study, a cover was used to protect the raw surface and produce a shorter transition between the SSD-free matrix and the original surface. The position of the mask was optimized via plasma simulation.

SiC was chosen as the cover material considering that a highly reactive and high-temperature plasma jet is needed to prevent the introduction of new contamination. Furthermore, a demonstration of rapid SSD detection was performed to help understand the influence of several lapping parameters.

2. Experimental setup

2.1. Materials

Single-crystal Si slices ($40 \times 40 \text{ mm}$) were used to study the single spot etching behavior of ICP. Commercially available on-axis sliced and epi-ready 4H-SiC wafers (SICC Co., Ltd, Shandong, China) were used in this study, and the thicknesses were $650 \mu\text{m}$ and $370 \mu\text{m}$, respectively. The wafers were cut into $10 \times 10 \text{ mm}$ slices. All experiments were conducted on the Si (0001) face, which is the most commonly used face for electronic device applications [28].

2.2. ICPE

The ICPE process was performed on the apparatus shown in figure 1(a). A three-channel gas supporting system is connected to a quartz torch, which consists of three concentric tubes. The inner tube is supplied with reactive gas, which is a mixture of CF_4 and oxygen in this case. The addition of oxygen can greatly reduce the deposition of fluorocarbons on the surface [29]. The second tube is supplied with pure argon at a flow rate of 1.5 slm as the plasma ignition gas. The outer tube is supplied with cooling gas, which is pure argon at a flow rate of 18 slm. The bottom part of the quartz torch is placed concentrically in an inductance coil. This inductance coil is connected to a matcher, which is connected to radio frequency (RF) power (27.12 MHz, 1000 W). During operation, the RF power generates an RF changing electronic field in the center of the inductance coil, which excites the gas passing through the coil and transforms it into a dense plasma jet. The sample to be etched is placed on a thermal insulation platform wafer holder that is connected to a three-axis numerical control (NC) platform. As shown in figure 1(b), the entire ICPE device is installed inside an enclosed metal chamber with an electromagnetic interference shielded window and connected to a ventilation system to prevent possible health damage from electromagnetic radiation and toxic exhaust.

2.3. The numerical simulation of atmospheric ICP torch

To have a better understanding of the temperature and velocity distribution of the ICP jet, we did a numerical simulation of atmospheric ICP torch conducted by COMSOL Multiphysics 5.4. In the case of atmosphere pressure, inductively coupled plasma is assumed to be under local thermodynamic equilibrium conditions. Hence, it can become a conductive fluid through interactions with electromagnetic fields in the simulation. Many assumptions were made to reduce the computational cost.

We combine the Navier–Stokes, heat, and Maxwell equations to describe the motion of the conducting fluid in

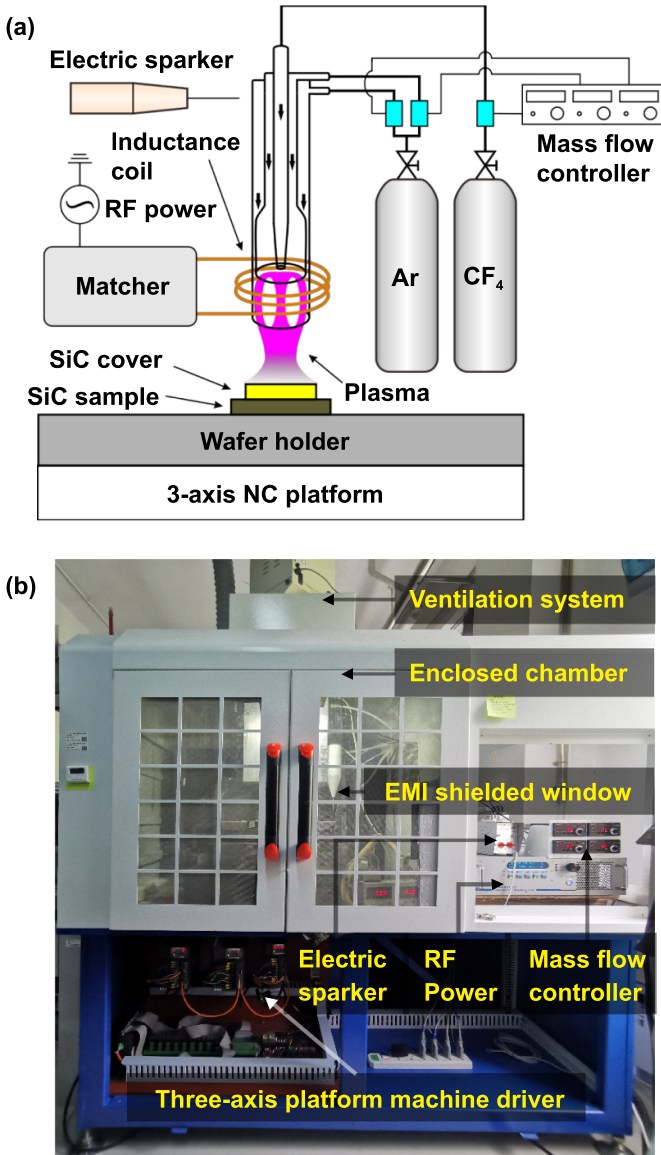


Figure 1. Experimental setup for ICP etching: (a) schematic diagram; (b) photograph.

an electromagnetic field. The governing equations of the torch model are summarized as follows:

The Navier–Stokes equations for laminar flow module:

Conservation of mass:

$$\nabla \cdot (\rho \mathbf{u}) = 0 \quad (1)$$

Momentum conservation equation:

$$\rho \frac{\partial \mathbf{u}}{\partial t} + \rho (\mathbf{u} \cdot \nabla) \mathbf{u} = \nabla \cdot \left[-p\mathbf{I} + \mu \left(\nabla \mathbf{u} + (\nabla \mathbf{u})^T \right) - \frac{2}{3} \mu (\nabla \cdot \mathbf{u}) \mathbf{I} \right] + \mathbf{F} \quad (2)$$

$$\mathbf{F} = \mathbf{j} \times \mathbf{B} \quad (3)$$

where ρ is the fluid density, \mathbf{u} is the velocity vector, p is the pressure, μ is the dynamic viscosity of the fluid, \mathbf{I} is the identity matrix, and \mathbf{F} is the Lorentz force acting on the fluid.

The heat transfer equation for heavy particles:

$$\rho C_p \frac{\partial T}{\partial t} + \rho C_p \mathbf{u} \cdot \nabla T - \nabla \cdot (k \nabla T) = Q \quad (4)$$

where Q is the heat source, T is the temperature, C_p is the specific heat capacity, k is the thermal conductivity.

$$Q = \frac{\partial}{\partial T} \left(\frac{5k_B T}{2q} \right) (\nabla T \cdot \mathbf{J}) + \mathbf{E} \cdot \mathbf{J} + Q_{\text{rad}} \quad (5)$$

The first term represents the enthalpy transport, the second term represents the joule heating, and Q_{rad} is the volumetric net radiation loss.

Maxwell equations were used to solve the magnetic field:

$$\nabla \times \mathbf{H} = \mathbf{J} \quad (6)$$

$$\mathbf{B} = \nabla \times \mathbf{A} \quad (7)$$

$$\mathbf{J} = \sigma \mathbf{E} + \mathbf{j} \omega \mathbf{D} + \sigma \nabla \times \mathbf{B} + \mathbf{J}_e \quad (8)$$

$$\mathbf{E} = -\mathbf{j} \omega \mathbf{A} \quad (9)$$

where \mathbf{H} is the magnetic field, \mathbf{J} is the plasma current density, \mathbf{B} is the magnetic flux density, \mathbf{A} is the potential vector, σ is the electrical conductivity, \mathbf{E} is the RF electric field, ω is the angular frequency, and \mathbf{D} is the displacement current.

Equations (1)–(9) were solved by a finite element method based on COMSOL software. The ICP torch is modeled to be a fully axisymmetric configuration, which is shown in figure 2. The ICP simulation uses the same model size and etching parameters as the experiment. The temperature of the quartz tube and the temperature of the ambient air are assumed to be 300 K under atmospheric pressure. The temperature data were collected from the exposed upper surface of the SiC sample. The velocity data were collected above the aforementioned surface with a distance of 0.01 mm.

2.4. SSD screening demonstration

A set of samples was prepared using various lapping parameters to demonstrate the rapid SSD screening ability of the ICPE method and to obtain the optimized lapping parameters for a high MRR with low SSD thickness. Lapping experiments were performed on the Si face of the epi-ready SiC substrate using diamond lapping discs of 500–3000 grits. All experiments were conducted using a metallographic grinding polishing machine from Laizhou Weiyi Experimental Machinery Manufacture Co., Ltd. The detailed lapping parameters are listed in table 1.

2.5. Characterization and measurement

Optical emission spectrometry (OES, Ocean optics USE4000) was used to determine the composition of radicals in the

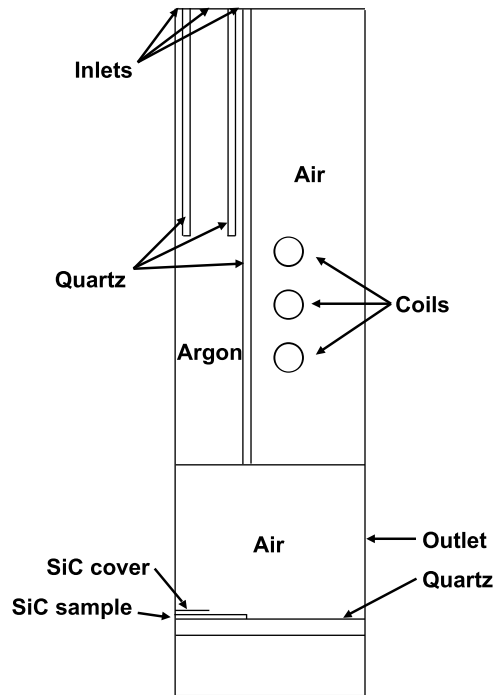


Figure 2. Schematic diagram of the geometry of the atmospheric ICP torch model.

Table 1. Parameters used in the lapping of SiC.

Parameters	Values
Lapping discs diameter	250 mm
Grit	500–3000 #
Pressure	50–200 kPa
Revolution speed	50–200 rpm
Time	2 min

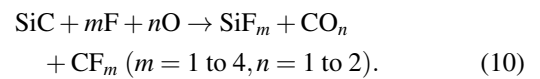
plasma. Confocal laser scanning microscopy (CLSM, KEYENCE VK-X1000) was applied to observe the morphology change along the etching spot and measure the depth of the SSD layer. Analytical balances (METTLER TOLEDO XSR105) were used to measure the MRR via mass difference. A profilometer (SURFCOM NEX 031) was used to measure the profile changes of the sample before and after ICPE. Scanning electron microscopy (SEM, ZEISS merlin) was employed to obtain more information about the surface morphology of the sample. Scanning transmission electron microscopy (STEM, Tecnai F30) was utilized to directly observe the SSD layer and measure the depth as a comparison test. The STEM sample was prepared by a focused ion beam (FIB, FEI Helios 600i).

3. Results and discussions

3.1. Plasma diagnostics

In this method, ICPE was the chosen approach for removing materials from the substrate surface and forming a taper that serves as the window for measuring the SSD depth. The ICPE of SiC should be a pure chemical process without mechanical

force and, thus, does not introduce new SSD, ensuring accurate SSD measurements. The process is based on the chemical reaction expressed as equation (10) [30]:



The reactive plasma must contain sufficient amounts of F and O radicals to ensure that the reaction progresses. Thus, plasma diagnostics of ICP were implemented before the etching operation. An optical photo of the ICP jet is shown in figure 3(a). OES was used to confirm the presence of etching radical compositions in the plasma. OES data were collected from the normal analysis zone of the ICP jet, and the results are shown in figure 3(b). When CF_4 was added to the plasma, distinctive peaks corresponding to CF_x and the typical C_2 swan system were observed [31–33]. The peaks representing fluorine radicals are difficult to detect because they overlap with the strong peaks of argon emissions. However, the strong peaks of CF_x and C_2 prove the sufficient dissociation of CF_4 , which generates a substantial amount of fluorine radicals as another major product [34]. The atomic oxygen peaks at 777 nm and 844 nm represent the transitions $\text{O} (3p5P \rightarrow 3s5S)$ and $\text{O} (3p3P \rightarrow 3s3S)$, respectively [35]. The OES results indicate that this ICP jet contains abundant F and O radicals that are capable of etching SiC.

3.2. Etching characteristics

The etching behavior of ICP was studied to make it a predictable tool for taper fabrication. Here, a 40×40 Si slice was used to explore the profile change of ICP torch etching. A single spot was etched on Si for 2 min. Optical photos of the samples are shown in figure 4(a), where 1 is the as-received sample, and 2 is the sample after single spot etching by ICP. The size of the ICPE pits is approximately 3 cm. Since we used an ICP torch with a diameter below 2 cm, the larger etching pits are due to the deflection of the plasma jet when it hits the sample surface and the flow and diffusion of radical. The cross-sectional profile of 1 and 2 along the diagonal is shown in figure 4(b). The profile change exceeds the size of the etching pits and stretches to the entire surface. Because of reaction consumption, a limited lifetime, and dilution by air, the concentration of etching radicals decreases as the distance from the torch increases. Thus, the etching depth decreases along the pit radius.

More detailed high magnification photos are shown in figures 4(c)–(f). Figures 4(c) and (d) show areas A and B of the etched sample, where A is the center of the etching pit and B is the edge of the etching pit. The initial rough and damaged surface cannot be observed in the CLSM image of area A, implying a thorough etching of the SSD layer. The opening of cracks can be observed in area B, suggesting that less complete etching occurred at the edge of the pit due to the lower concentration of etching radicals. Figures 4(e)–(f) shows the area outside the etching pit. The yellow and gray

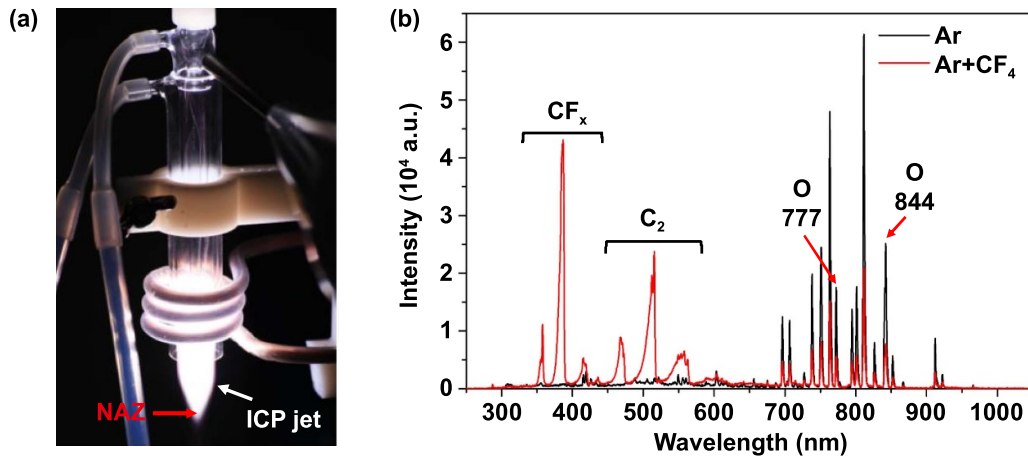


Figure 3. (a) Optical photo of the ICP jet; (b) OES spectra of the ICP jet with and without CF_4 addition.

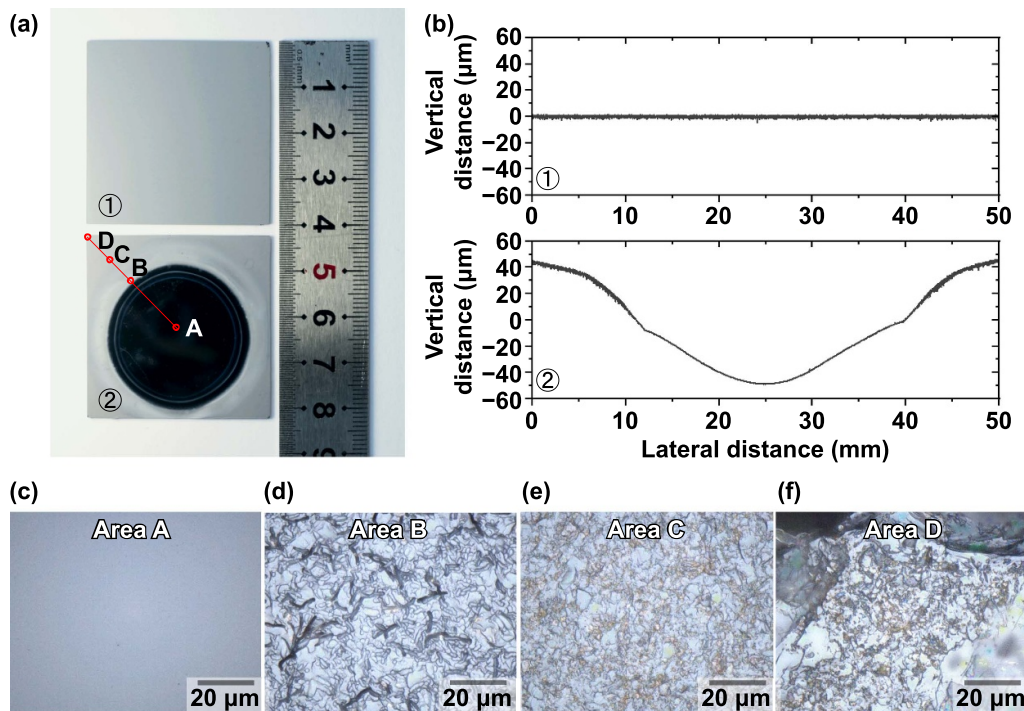


Figure 4. (a) Optical photo of the ICP etching samples: 1. As-received sample, 2. Etched sample; (b) the cross-section profile along the diagonal of samples 1 and 2, respectively; (c)–(f) the CLSM image of area A–D in figure (a) respectively.

particles on the surface area should be the deposited fluorocarbon polymers [36]. This result could explain the profile change outside the etching pits, where accumulated fluorocarbon polymer covers the initial surface. Furthermore, the adsorption of deposited particles increases with decreasing temperature, which has a consistent trend with the distance from the heat source, i.e. the plasma center. Consequently, the entire initial surface of the sample will be deformed, either by etching from plasma or occlusion by deposition particles, and it is impracticable to identify the raw surface after unobstructed etching. Nevertheless, marking the position of the raw surface is crucial in destructive SSD detection; hence,

a raw surface protective countermeasure is needed during ICPE [13].

3.3. SSD detection

Masks of photoresist or deposited metal are often used in the plasma etching process to protect certain areas. In this study, a mask was used for that purpose. To resist the high temperature and highly reactive radicals from the ICP torch, a slice of 4H-SiC was used as the mask.

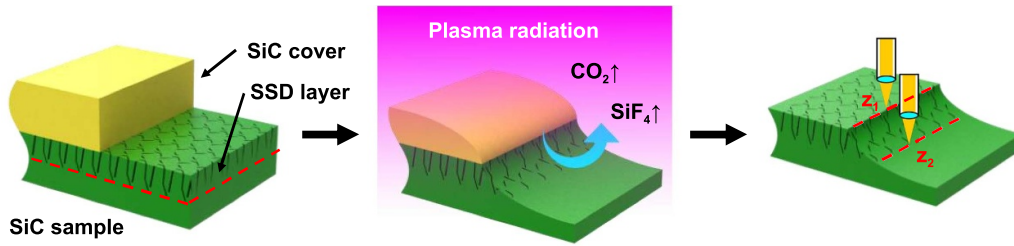


Figure 5. Schematic diagram of the SSD detection process.

The entire rapid SSD measurement process is listed as follows: (a) ICP is ignited as described in section 2. (b) As illustrated in figure 5, the SiC sample for the SSD measurement is partially covered by a smaller piece of SiC to protect a portion of the original surface as a reference plane to measure the SSD depth. (c) The covered sample is then moved directly under the ICP flame by the three-axis NC platform and etched for 2 min. (d) After etching, the SiC cover is released, and the etched SiC sample is cleaned with DI water and alcohol. (e) After cleaning, the etching profile is observed via CLSM. The depth of the SSD layer is obtained by comparing the vertical distance between the protected original surface (z_1) and the last trace of the SSD layer (z_2).

A taper that gradually deepens is needed to observe the SSD depth successfully. Considering the ease of CLSM operation and avoiding stitching measurement to ensure accuracy, the lateral length of the taper should be controlled within $100 \mu\text{m}$. Moreover, the etching rate should increase along the exposed sample surface and cover the $100 \mu\text{m}$ observation zone mentioned above. The etching rate is governed by the Arrhenius equation listed in equation (11):

$$v = n_F A \exp\left(\frac{-Ea}{RT}\right) \quad (11)$$

where n_F is the concentration of fluorine radicals on the surface, A is the pre-exponential factor, Ea is the activation energy of the etching reaction, R is the universal gas constant, and T is the absolute temperature of the sample surface. For this specific reaction, A , Ea , and R are constant values. Thus, we only need to study the temperature and radical concentration. According to figure 4, the lateral distance between the plasma center and the sample (d_{p-s}) significantly affects the etching behavior. Hence, we studied the influence of d_{p-s} on these two factors that affect the etching rate using COMSOL Multiphysics.

Figures 6(a)–(c) show the temperature simulation of the etching process for three sample positions in which d_{p-s} equals 0.5 mm, 5 mm, and 9 mm, respectively. Figure 6(d) shows the temperature of the observation zone, which is on the surface of the sample and ranges from the mask boundary to the

exposed part of the sample $100 \mu\text{m}$ away horizontally. With increasing d_{p-s} , the sample moves to the edge of the plasma, and the temperature gradually decreases. However, the temperature of each sample is uniform, fluctuating within 1°C . This result might be due to the excellent thermal conductivity of SiC. Thus, the etching rate difference due to temperature change can be neglected. As the calculation of the reactive radical concentration on the surface can be complicated, we studied the flow rate of the plasma as an approximation to facilitate the investigation. Figures 6(e)–(g) show the simulation of the flow rate of the three experiments. The flow rate on the sample surface should be zero. Here we chose the flow rate from the area $10 \mu\text{m}$ above the observation zone, the aforementioned indicator of the flow condition near the surface, and the data are plotted in figure 6(h). The velocity variation increases with d_{p-s} . A larger flow rate change induces a larger etching rate difference. Accordingly, the sample stack should be placed in the outer region of the plasma, and $d_{p-s} = 9 \text{ mm}$ was used in the subsequent experiments.

ICPE for SSD measurement was conducted on the Si face of the SiC sample with an SiC cover and $d_{p-s} = 9 \text{ mm}$. The morphology changes before and after etching are shown in figure 7. The lapped SiC surface (figure 7(a)) shows an actinomorphic trajectory pattern, which is caused by the periodic eccentricity lapping process [37]. Figure 7(b) shows the same sample after SSD reveals etching. The left part is the covered area, where no visual difference can be observed. The right part is the etched area, where a glazed surface implies the removal of the damaged layer. A distinctive boundary is observed between the covered and etched areas. Figure 7(c) is a schematic of the etching boundary area, which is marked by the red rectangle in figure 7(b). The red arrows 1–3 represent the covered area, transition etched area, and through-out etched area, which are shown in figures 7(e)–(g), respectively. Figure 7(d) is the SEM image of the original surface. No discrepancy can be observed within the area of the etched SiC sample under the protection of the SiC cover (figure 7(e)), which indicates that the SiC cover efficiently suppresses the etching of SiC beneath it. Thus, the surface under the SiC cover can be used as a reliable initial reference plane for measuring the thickness of the SSD layer. Figure 7(f) shows the area near the edge of the SiC cover, where radical flow can reach

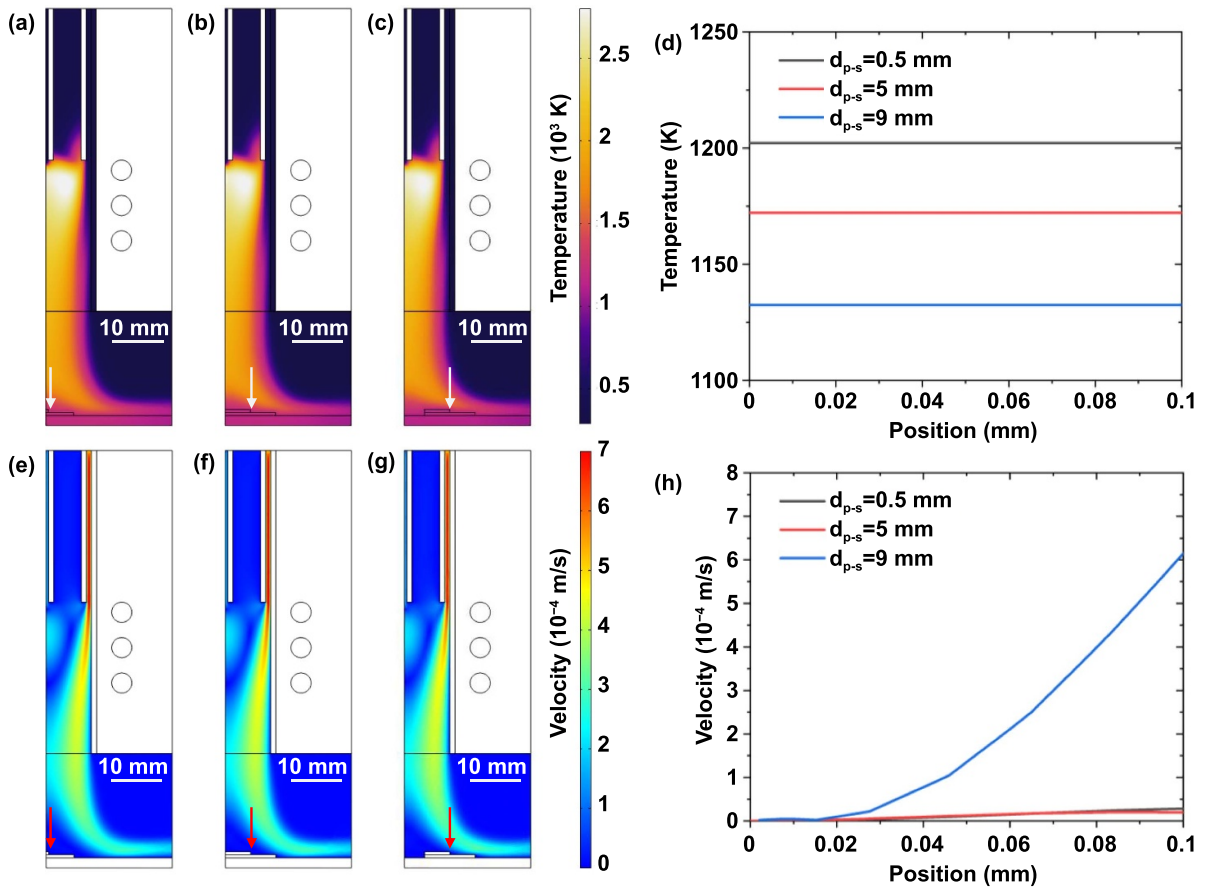


Figure 6. (a)–(d) Temperature simulation of the ICP torch, the color legend of (a)–(c) is shown to the right of (c); (e)–(h) flow velocity simulation the ICP torch, the color legend of (e)–(g) is shown to the right of (g).

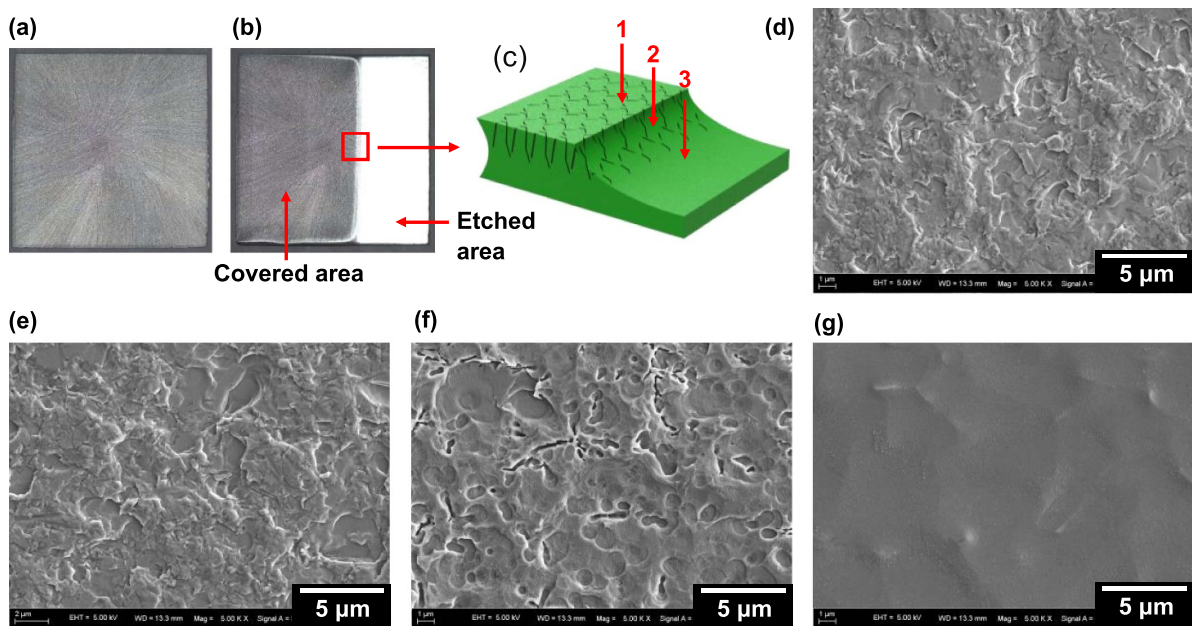


Figure 7. The optical photo of the (a) as received lapping SiC and (b) etched SiC; (c) the schematic diagram of the etching boundary in (b); SEM micrograph of (d) as received sliced SiC surface; (e) area 1 under the protection of SiC cover after etching; (f) area 2 near the boundary of SiC cover and (g) area 3 without the protection of SiC cover.

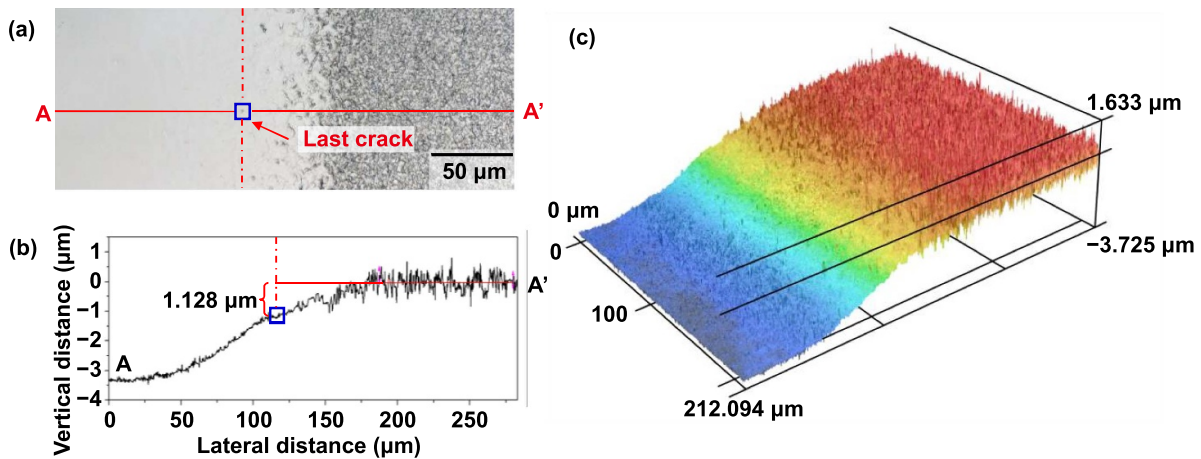


Figure 8. (a) the CLSM image of the etched slope of the sliced SiC sample; (b) the cross-sectional profile along A–A'; (c) the 3D image of (a).

and react with the sliced SiC sample surface. Meanwhile, the edge of the SiC cover confines the radical flow from some directions; thus, the SSD layer is only partially removed. Many cracks are revealed by the plasma etching, suggesting that the revealed plane is inside the SSD layer. Figure 7(g) shows the surface of the sliced SiC sample far from the protection of the SiC cover. Without any protection, the SSD layer is fully etched. Cracks completely vanish on the surface, indicating that the surface is damage-free [13]. The island structure remaining on the surface is caused by the uneven etching rate between the damaged layer and damage-free matrix [38]. ICPE in this part crossed the bottom of the SSD layer.

To measure the vertical distance between the original surface and the bottom of the SSD layer, CLSM was employed, and the results are shown in figure 8. The 2D CLSM image is shown in figure 8(a), and the 3D image is shown in figure 8(c). A very clean taper was formed via ICPE. For figures 8(a) and (b), the left side of the SiC sample exploded under ICP, while the right side was under the protection of the SiC cover. The right side retained its original morphology, suggesting that no etching occurred in this area, which agrees with the SEM result in figure 7(e). The left side underwent etching of dense ICP, and the original morphology was totally removed. A slope structure caused by the partial protection of the SiC cover edge links the original surface and deeply etched area. A gradual reduction in crack density can be observed along the taper, analogous to that of the MRF taper method, representing thinning of the SSD layer [39]. The deepest crack disappears in the bottom of the SSD layer. After that spot, all SSDs were removed, and only perfect SiC remained. A cross-sectional profile was extracted along the last crack trace, as depicted in figure 8(b). The blue rectangle in figure 8(b) indicates the position of the last crack. The vertical distance to the original surface is $1.128 \mu\text{m}$, which is also the depth of the SSD layer. figure 8(b) also demonstrates that the total etching depth is approximately $4 \mu\text{m}$, which is more than three times

the measured SSD layer thickness. In this case, the etching depth is sufficient to penetrate the SSD layer, suggesting that the result is accurate.

To further confirm the accuracy of the SSD measurement, FIB was used to cut a cross section of the etched sample, and STEM was employed to directly observe the SSD layer. Figure 9(a) shows the area under the protection of the SiC cover: Cracks, stress and amorphous layers can be clearly observed. The depth of the SSD layer is approximately $1.06 \mu\text{m}$, which matches the ICPE sample. Higher magnification images of areas A and B are shown in figures 9(b) and (c), which represent the typical crack region and deformed region of the SSD layer. The cross section of the part where SSDs are fully removed by ICPE is depicted in figure 9(d). A visually uniform SiC interface was observed, indicating that the SSD layer was removed. The high resolution transmission electron microscope (HRTEM) of the interface region shown in figure 9(e) further proves this point. Perfectly crystalline 4H-SiC was observed immediately below the interface, and the image corresponds to the $\langle 11-20 \rangle$ face of 4H-SiC [40]. This result proves that only single crystal 4H-SiC remained on the crack-free surface formed by ICPE, and no new SSD was introduced. The selected area electron diffraction (SAED) pattern in figure 9(f) shows a typical diffraction pattern along the $[11-20]$ zone axis of 4H-SiC, which agrees with the HRTEM image and further supports the good crystallinity of the remaining substrate [41]. The results demonstrate that ICPE of SiC is a rapid, SSD-free method that produces accurate SSD measurements, making it a promising approach for SSD detection of SiC.

3.4. Rapid SSD screening demonstration

The ability of the ICPE method to rapidly and accurately detect the thickness of the SSD layer enables us to quickly screen and find the optimal lapping parameters. Here, we demonstrate

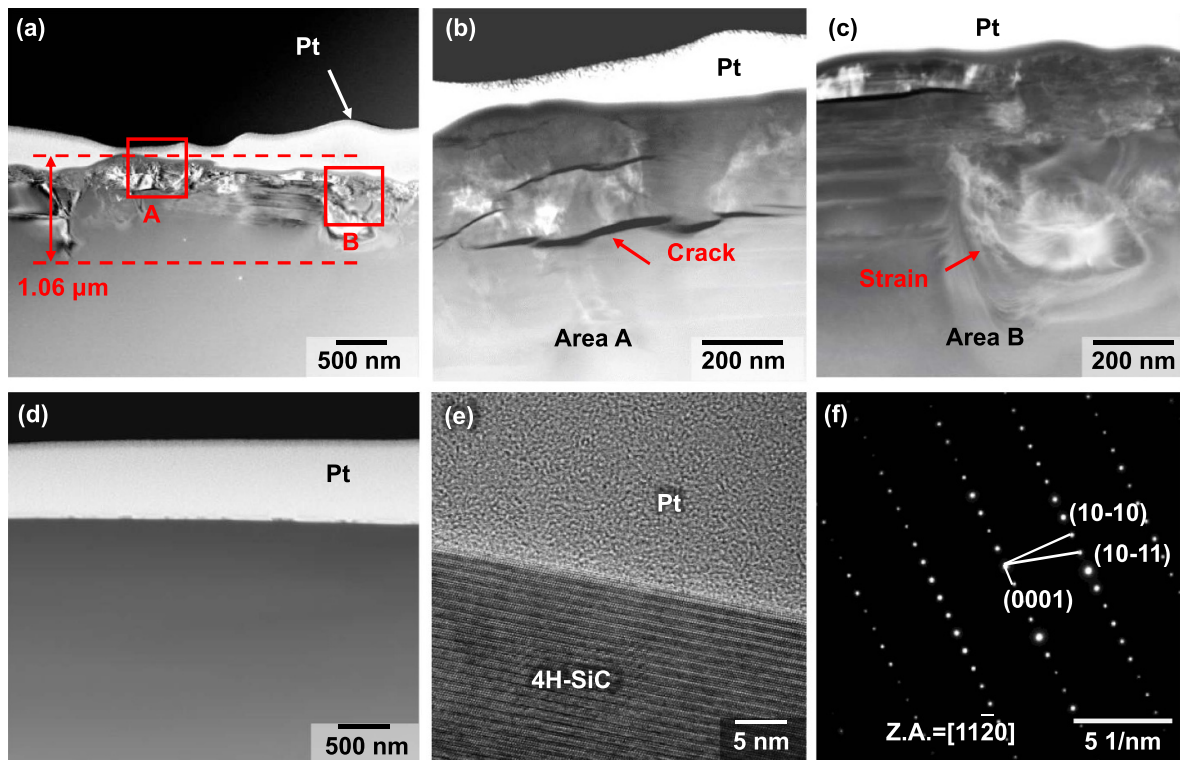


Figure 9. Subsurface investigation performed by STEM: (a)–(c) STEM images of the as-ground SiC surface, obtained with different magnifications; (d) STEM image of the ICP etched SiC surface; (e) HRTEM image of the ICP etched SiC surface; (f) selected area electron diffraction pattern of the ICP etched SiC surface.

Table 2. Lapping parameters for SSD detection.

#	Pressure (kPa)	Granularity (mesh #)	Revolution velocity (rpm)
1	50	1000	150
2	100	1000	150
3	150	1000	150
4	200	1000	150
5	50	500	150
6	50	1000	150
7	50	2000	150
8	50	3000	150
9	50	1000	50
10	50	1000	100
11	50	1000	150
12	50	1000	200

this rapid screening ability using ICPE to study the influence of lapping parameters, including granularity, lapping pressure, and revolution velocity. Twelve sets of samples were lapped using the parameters listed in table 2.

With the assistance of rapid ICPE, only 2 min of etching are needed to reveal the SSD layer of each sample. Meanwhile, the system operates in an atmospheric environment, which eliminates time-consuming vacuum process in normal plasma etching. In addition, this method does not require a subsequent

etching step for opening cracks, which is indispensable for the traditional MRF method. Furthermore, the NC platform can load multiple samples. The entire SSD revelation process for 12 samples is completed within 30 min.

Figure 10(a) shows the influence of lapping pressure on the MRR and SSD of the SiC sample (sample number 1–4). MRR increases linearly with increasing pressure. However, the SSD changes at a much lower rate because the gap between the sample and diamond disc decreases with increasing lapping pressure. The number of abrasive particles that undertake the load also increases, so the contact pressure remains constant. This causes the relevant SSD thickness to remain constant [42]. However, the MRR increases quickly as the number of effective abrasive particles increases. Granularity has a similar influence over the MRR and SSD layers (sample number 5–8), as shown in figure 10(b). This is because grain size directly affects the cut depth of each grain. In figure 10(c), representing sample number 9–12, the MRR increases with the revolution velocity because a higher cutting speed removes more material in unit time. However, if cut depth remains the same, no obvious change trend of SSD can be observed, which means that SSD is not sensitive to lapping revolution velocity. In summary, granularity has the greatest effect on SSD thickness, followed by pressure. Revolution velocity has no clear influence on SSD thickness.

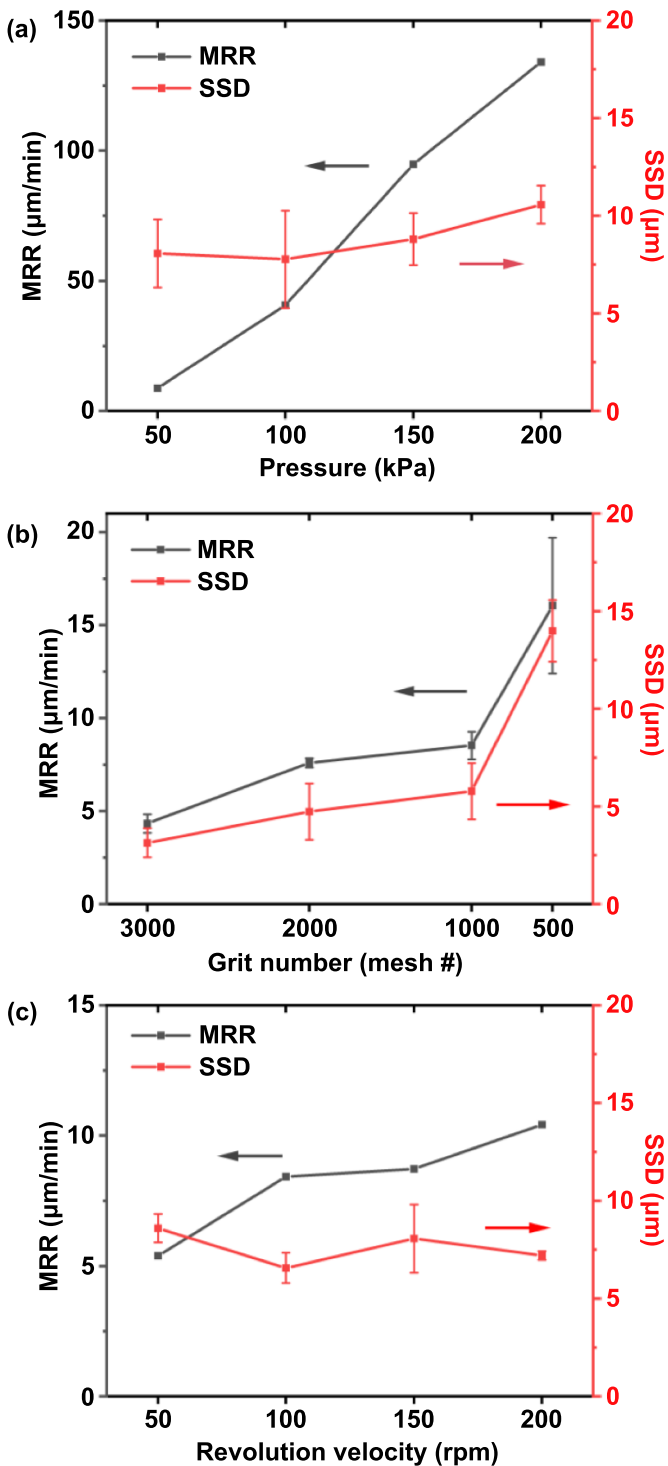


Figure 10. Influence of (a) pressure (sample number 1–4), (b) granularity (sample number 5–8), and (c) revolution velocity (sample number 9–12) on SSD and MRR of SiC.

4. Conclusion

Atmospheric ICPE, an SSD-free material removal method, was used to perform rapid SSD detection of SiC. The plasma diagnosis and etching behavior study showed its capability for fast material removal. Plasma flow simulation was used to optimize the etching position, and rapid SSD detection

finished within 2 min. As confirmed via STEM, the ICPE process did not introduce new SSD, and the SSD layer thickness determined by STEM matched well with that of the ICPE method. A demonstration of rapid scanning was demonstrated on 12 samples to study the influence of lapping parameters on SSD. The results indicate that ICPE is a promising SSD detection method. It is rational to further propose that by altering the composition of the etching gas, ICPE could be a general method for SSD detection in a wide range of materials.

Acknowledgments

This project is supported by the National Natural Science Foundation of China (52035009, 52005243) and the Science and Technology Innovation Committee of Shenzhen Municipality (JCYJ20200109141003910, GJHZ20180928155412525). The authors acknowledge the assistance of SUSTech Core Research Facilities.

ORCID iD

Hui Deng  <https://orcid.org/0000-0002-7116-7188>

References

- [1] Naftaly M, Molloy J F, Magnusson B, Andreev Y M and Lanski G V 2016 Silicon carbide—a high-transparency nonlinear material for THz applications *Opt. Express* **24** 2590–5
- [2] Nakamura D, Gunjishima I, Yamaguchi S, Ito T, Okamoto A, Kondo H, Onda S and Takatori K 2004 Ultrahigh-quality silicon carbide single crystals *Nature* **430** 1009–12
- [3] Lee S P, Shin Y S, Bae D S, Min B H, Park J S and Kohyama A 2006 Fabrication of liquid phase sintered SiC materials and their characterization *Fusion Eng. Des.* **81** 963–7
- [4] Kitahara H, Noda Y, Yoshida F, Nakashima H, Shinohara N and Abe H 2001 Mechanical behavior of single crystalline and polycrystalline silicon carbides evaluated by Vickers indentation *J. Ceram. Soc. Japan* **109** 602–6
- [5] Zhang Z Y, Yan J W and Kuriyagawa T 2011 Study on tool wear characteristics in diamond turning of reaction-bonded silicon carbide *Int. J. Adv. Manuf. Technol.* **57** 117–25
- [6] Bude J et al 2014 High fluence laser damage precursors and their mitigation in fused silica *Opt. Express* **22** 5839–51
- [7] Gao F and Weber W J 2004 Mechanical properties and elastic constants due to damage accumulation and amorphization in SiC *Phys. Rev. B* **69** 224108
- [8] Dessemond L and Kleitz M 1992 Effects of mechanical damage on the electrical properties of zirconia ceramics *J. Eur. Ceram. Soc.* **9** 35–9
- [9] Neslen C L, Mitchel W C and Hengehold R L 2001 Effects of process parameter variations on the removal rate in chemical mechanical polishing of 4H-SiC *J. Electron. Mater.* **30** 1271–5
- [10] Hu Y, Shi D, Hu Y, Zhao H W and Sun X D 2018 Investigation on the material removal and surface generation of a single crystal SiC wafer by ultrasonic chemical mechanical polishing combined with ultrasonic lapping *Materials* **11** 2022
- [11] Song X L, Li Y K, Jiang N, Qu Y X and Qiu G Z 2008 Recent development of chemical mechanical polishing *Chem. Ind. Eng. Prog.* **27** 26–31

- [12] Speed D *et al* 2015 Physical, chemical, and *in vitro* toxicological characterization of nanoparticles in chemical mechanical planarization suspensions used in the semiconductor industry: towards environmental health and safety assessments *Environ. Sci. Nano* **2** 227–44
- [13] Yin J F, Bai Q and Zhang B 2018 Methods for detection of subsurface damage: a review *Chin. J. Mech. Eng.* **31** 41
- [14] Lee Y 2011 Evaluating subsurface damage in optical glasses *J. Eur. Opt. Soc.* **6** 11001
- [15] Suratwala T, Wong L, Miller P, Feit M D, Menapace J, Steele R, Davis P and Walmer D 2006 Sub-surface mechanical damage distributions during grinding of fused silica *J. Non-Cryst. Solids* **352** 5601–17
- [16] Neauport J, Ambard C, Cormont P, Darbois N, Destribats J, Luitot C and Rondeau O 2009 Subsurface damage measurement of ground fused silica parts by HF etching techniques *Opt. Express* **17** 20448–56
- [17] Lakhdari F, Bouzid D, Belkhir N and Herold V 2017 Surface and subsurface damage in Zerodur® glass ceramic during ultrasonic assisted grinding *Int. J. Adv. Manuf. Technol.* **90** 1993–2000
- [18] Zhuang D and Edgar J H 2005 Wet etching of GaN, AlN, and SiC: a review *Mater. Sci. Eng. R* **48** 1–46
- [19] Chen S S, Li S Y, Peng X Q, Hu H and Tie G P 2015 Research of polishing process to control the iron contamination on the magnetorheological finished KDP crystal surface *Appl. Opt.* **54** 1478–84
- [20] Cheng H B, Feng Z J, Wang Y W and Lei S T 2005 Magnetorheological finishing of SiC aspheric mirrors *Mater. Manuf. Processes.* **20** 917–31
- [21] Lambropoulos J C, Salzman S, Smith T R, Xu J, Pomerantz M, Shanmugam P, Davies M A, Taylor L L and Qiao J 2017 Subsurface Damage (SSD) Assessment in Ground Silicon Carbide (SiC) (9–13 July 2017) (Denver: Colorado Optical Fabrication and Testing 2017) p OM3B.5
- [22] Cardinaud C, Peignon M-C and Tessier P-Y 2000 Plasma etching: principles, mechanisms, application to micro- and nano-technologies *Appl. Surf. Sci.* **164** 72–83
- [23] Bárdos L and Baránková H 2008 Plasma processes at atmospheric and low pressures *Vacuum* **83** 522–7
- [24] Fanara C, Shore P, Nicholls J R, Lyford N, Kelley J, Carr J and Sommer P 2006 A new reactive atom plasma technology (RAPT) for precision machining: the etching of ULE® surfaces *Adv. Eng. Mater.* **8** 933–9
- [25] Jin H L, Xin Q, Li N, Jin J, Wang B and Yao Y X 2013 The morphology and chemistry evolution of fused silica surface after Ar/CF₄ atmospheric pressure plasma processing *Appl. Surf. Sci.* **286** 405–11
- [26] Dai Z C, Chen S Y, Xie X H and Zhou L 2019 Investigation of grinding and lapping surface damage evolution of fused silica by inductively coupled plasma etching *Int. J. Precis. Eng. Manuf.* **20** 1311–23
- [27] Novak M and Sharma D 2013 3D optical microscopes: a basic technology comparison for metrology applications: learn more about 3D techniques such as white light interferometry and confocal microscopy (BNP Media) **52** 30–3 (<https://www.proquest.com/scholarly-journals/3-d-optical-microscopes-basic-technology/docview/1348254625/se-2?accountid=162699>)
- [28] Zhang Y, Li R L, Zhang Y J, Liu D Z and Deng H 2019 Indiscriminate revelation of dislocations in single crystal SiC by inductively coupled plasma etching *J. Eur. Ceram. Soc.* **39** 2831–8
- [29] Sun R Y, Yang X, Watanabe K, Miyazaki S, Fukano T, Kitada M, Arima K, Kawai K and Yamamura K 2019 Etching characteristics of quartz crystal wafers using argon-based atmospheric pressure CF₄ plasma stabilized by ethanol addition *Nanomanuf. Metrol.* **2** 168–76
- [30] Yih P H, Saxena V and Steckl A J 1997 A review of SiC reactive ion etching in fluorinated plasmas *Phys. Status Solidi b* **202** 605–42
- [31] Omori N, Matsuo H, Watanabe S and Puschmann M 1996 Influence of carbon monoxide gas on silicon dioxide dry etching *Surf. Sci.* **352–354** 988–92
- [32] Wang R X, Zhang C, Liu X, Xie Q, Yan P and Shao T 2015 Microsecond pulse driven Ar/CF₄ plasma jet for polymethylmethacrylate surface modification at atmospheric pressure *Appl. Surf. Sci.* **328** 509–15
- [33] Jung T Y, Kim D H and Lim H B 2006 Molecular emission of CF₄ gas in low-pressure inductively coupled plasma *Bull. Korean Chem. Soc.* **27** 373–5
- [34] Zimmermann S, Ahner N, Blaschta F, Schaller M, Rülke H, Schulz S E and Gessner T 2010 Analysis of the impact of different additives during etch processes of dense and porous low-*k* with OES and QMS *Microelectron. Eng.* **87** 337–42
- [35] Zhou R W, Zhang X H, Zong Z C, Li J X, Yang Z B, Liu D P and Yang S Z 2015 Reactive oxygen species in plasma against *E. coli* cells survival rate *Chin. Phys. B* **24** 085201
- [36] Milella A, Palumbo F, Favia P, Cicala G and d'Agostino R 2004 Continuous and modulated deposition of fluorocarbon films from c-C₄F₈ plasmas *Plasma Process. Polym.* **1** 164–70
- [37] Li H N, Yang Y, Zhao Y J, Zhang Z L, Zhu W Q, Wang W L and Qi H 2019 On the periodicity of fixed-abrasive planetary lapping based on a generic model *J. Manuf. Process.* **44** 271–87
- [38] Johnson W A, North J C and Wolfe R 1973 Differential etching of ion-implanted garnet *J. Appl. Phys.* **44** 4753–7
- [39] Menapace J A, Davis P J, Steele W A, Wong L L, Suratwala T I and Miller P E 2006 MRF applications: measurement of process-dependent subsurface damage in optical materials using the MRF wedge technique *Proc. SPIE 5991, Laser-Induced Damage in Optical Materials: 2005* (Boulder, CO: SPIE) p 599103
- [40] Calabretta C, Agati M, Zimbone M, Boninelli S, Castiello A, Pecora A, Fortunato G, Calcagno L, Torrisi L and La Via F 2019 Laser annealing of P and Al implanted 4H-SiC epitaxial layers *Materials* **12** 3362
- [41] Dobrzhinetskaya L, Mukhin P, Wang Q, Wirth R, O'Bannon E, Zhao W X, Eppelbaum L and Sokhonchuk T 2018 Moissanite (SiC) with metal-silicide and silicon inclusions from tuff of Israel: Raman spectroscopy and electron microscope studies *Lithos* **310–311** 355–68
- [42] Wang Z, Wu Y L, Dai Y F, Li S Y and Zhou X S 2008 Rapid detection of subsurface damage of optical materials in lapping process and its influence regularity *Opt. Precis. Eng.* **1** 16–21